Axion-Field-Enhanced Near-Field Thermophotovoltaic Systems with Band Dislocation

Rongqian Wang[1], Jincheng Lu[2,3], Jiebin Peng[4,5*], and Jian-Hua Jiang[6,7,8*]

[1]*School of Physical Science and Technology & Collaborative Innovation Center of Suzhou Nano Science and Technology, Soochow University, Suzhou 215006, China*
[2]*Key Laboratory of Intelligent Optoelectronic Devices and Chips of Jiangsu Higher Education Institutions, School of Physical Science and Technology, Suzhou University of Science and Technology, Suzhou 215009, China*
[3]*Advanced Technology Research Institute of Taihu Photon Center, School of Physical Science and Technology, Suzhou University of Science and Technology, Suzhou 215009, China*
[4]*School of Physics and Optoelectronic Engineering, Guangdong University of Technology, Guangzhou 510006, China*
[5]*Guangdong Provincial Key Laboratory of Sensing Physics and System Integration Applications, Guangdong University of Technology, Guangzhou 510006, China*
[6]*School of Biomedical Engineering, Division of Life Sciences and Medicine, University of Science and Technology of China, Hefei 230026, China*
[7]*Suzhou Institute for Advanced Research, University of Science and Technology of China, Suzhou 215123, China*
[8]*Department of Modern Physics, School of Physical Sciences, University of Science and Technology of China, Hefei 230026, China*

(Received 14 June 2025; accepted manuscript online 19 August 2025)

We propose a near-field thermophotovoltaic system utilizing magnetic Weyl semimetals, which exhibit a distinct gyrotropic effect originating from their intrinsic axion field. Critically, we demonstrate that intentional band dislocation, achieved by layer-specific tuning of the chemical potential, significantly enhances the energy-conversion efficiency. This effect arises from the formation of quasi-flat bands in momentum space, which broaden the spectral heat flux and amplify photon tunneling above the bandgap. At optimized chemical potential mismatches, the system achieves a 65% Carnot efficiency and a power density of $7\times10^4\ \mathrm{W\cdot m^{-2}}$, surpassing symmetric configurations by 7%. The optimization of the Weyl semimetals thickness further demonstrates a clear tuning window where both the output power and energy-conversion efficiency are significantly improved. These results establish chemical-potential engineering toward high-efficiency near-field thermophotovoltaics for waste heat recovery and infrared energy applications.

DOI: 10.1088/0256-307X/42/10/100403 CSTR: 32039.14.0256-307X.42.10.100403

1. Introduction. Thermophotovoltaic systems hold great promise for efficient energy conversion in applications ranging from solar energy harvesting to waste heat recovery.[1–6] By using a thermal emitter to radiate photons across a vacuum gap to a photovoltaic cell, thermophotovoltaic systems convert thermal energy into electricity via the photovoltaic effect.[7–13] While far-field thermophotovoltaic systems are limited by the Stefan–Boltzmann law, near-field thermophotovoltaic (NTPV) systems, where sub-wavelength gaps separate the emitter and the photovoltaic cell, can dramatically enhance the power density through evanescent wave coupling.[14–17]

NTPV systems achieve optimal efficiency when the energy bandgap (E_g) of the thermophotovoltaic cell is spectrally matched to the emitter's thermal radiation spectrum. To meet this requirement, Ⅲ-Ⅴ semiconductors with narrow bandgaps are commonly employed in thermophotovoltaic cell fabrication due to their strong infrared photon absorption.[18–26] Significant efforts have been devoted to ultilizing engineered materials that exploit surface polaritons, such as surface-plasmon polaritons,[27–30] surface-phonon polaritons,[31,32] or their hybrids.[33–35] These materials enable strong field confinement and spectral control, enhancing the radiative heat transfer and matching the emission spectrum to the bandgap of the photovoltaic cells. Periodic or layered structures incorporating these materials are also widely employed in NTPV systems to enhance their performance.[36–39] For example, reference [37] shows that a multilayer emitter enhances photocurrent generation and electric power in an NTPV cell compared to bulk tungsten. Reference [39] investigates an NFTPV system with a periodic multilayer hyperbolic metamaterial emitter, demonstrating an optimal output power of $1.22\times10^4\ \mathrm{W/m^2}$ at 900 K. Challenges remain in designing selective emitters with high emittance for photon energies larger than the bandgap while suppressing the below-gap radiation.[14,40]

Weyl semimetals, as a topologically nontrivial phase

*Corresponding authors. Email: jiebin.peng@gdut.edu.cn; jhjiang3@ustc.edu.cn
© 2025 Chinese Physical Society and IOP Publishing Ltd. All rights, including for text and data mining, AI training, and similar technologies, are reserved.

of matter, have recently attracted significant attention due to their massless bulk fermions and protected Fermi arc surface states, leading to unique topological transport phenomena.[41–43] Their band structure features an even number of nondegenerate band-touching points (Weyl nodes) in momentum space, which act as magnetic monopoles and antimonopoles with corresponding nonzero Chern numbers.[44–46] These exotic properties lead to highly asymmetric optical responses and non-reciprocal electromagnetic behavior, making Weyl semimetals promising candidates for NTPV applications.[47–50] Using the strong temperature dependence of their chemical potential and the significant nonreciprocity of their optical properties to exploit their high crystalline behavior, we design a system capable of achieving enhanced performance in near-field heat-to-electricity applications.

In this work, we propose an NTPV system using a sandwich structure composed of magnetic Weyl semimetals, where chemical potential tuning enables effective control of radiative heat flux and photocurrent. The lower chemical potentials enhance the energy-conversion efficiency through increased absorption and photocurrent generation, while higher values blueshift the resonance frequencies, reducing performance. We observe an efficiency enhancement effect due to the band dislocation in different configurations of chemical potentials. The optimized design achieves superior energy conversion efficiency, which makes magnetic Weyl semimetals promising platforms for advanced energy harvesting applications. The proposed system demonstrates significantly enhanced performance without requiring a large emitter-cell temperature gradient, thereby addressing a key technical limitation in current experimental implementations.[24,51,52] Unlike conventional solar cells, the developed NTPV system is specifically optimized for energy harvesting under small temperature differentials (near-ambient conditions).

2. System and Method. The proposed NTPV system is presented in Fig. 1(a). The emitter consists of two layers of Weyl semimetals separated by a dielectric layer with a permittivity of 2, kept at a temperature T_{e}. The thicknesses of the Weyl semimetals and dielectric layer are h_{WSM} and h_0, repsctively. The chemical potentials of the two layers of Weyl semimetals are denoted by $E_{\mathrm{f},1}$ and $E_{\mathrm{f},3}$, respectively. The thermophotovoltaic cell is made of an indium antimonide (InSb) p–n junction with thickness h_{InSb}, kept at a temperature T_{c}, and is covered by a structure identical to the emitter (two layers of Weyl semimetals with a dielectric layer in between). While electronic-level effects are not considered, our analysis focuses on optical interfacial modes around 1 Hz, where fluctuation electrodynamics fails to account for interfacial coupling effects at this scale.[36,53] The thermal radiation from the emitter is absorbed by the cell and converted to electricity via the photovoltaic effect.[42] Figure 1(b) shows the transmission coefficients for three distinct NTPV systems: (i) semi-infinite Weyl semimetals with matched chemical potential (top panel), (ii) thin-film Weyl semimetals with matched chemical potential (middle panel), and (iii) thin-film Weyl semimetals with chemical potential mismatch (bottom panel). The results clearly demonstrate the band dislocation effect, where a quasi-flat band (indicated by the white arrow in the bottom panel) emerges in momentum space, establishing an efficient heat transfer channel.

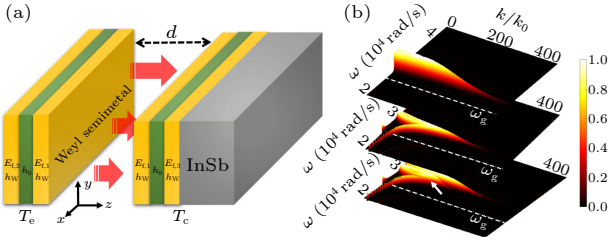

Fig. 1. (a) Schematic representation of the NTPV system. (b) Demonstration of the band dislocation effect. A thermal emitter of temperature T_{e}, consisting of two layers of Weyl semimetals separated by a dielectric layer with a permittivity of 2, is placed in the proximity of a thermophotovoltaic cell of temperature T_{c}. The cell is an InSb p–n junction, which is covered by an identical three-layer structure as the emitter. The emitter-cell distance is kept at d. h_{WSM} and h_0 are the thicknesses of the Weyl semimetals and dielectric layer, respectively. $E_{\mathrm{f},1}$ and $E_{\mathrm{f},3}$ represent the chemical potentials of the two layers of Weyl semimetals, respectively. The band dislocation effect occurs where a quasi-flat band (indicated by the white arrow in the bottom panel) emerges in momentum space.

While the anomalous Hall effect is more pronounced at low temperatures (though improving with rising temperatures), anisotropic and nonreciprocal photoresponses persist even at room temperature.[54] Here, we primarily focus on the room-temperature anisotropy and strong infrared photon coupling of Weyl semimetals, which enable surface electromagnetic modes.[43,45,55] These modes enhance near-field thermal radiation, while the multilayer design supports resonant energy exchange between the emitter and the absorber, optimizing radiative heat transfer. The identical emitter-absorber configuration promotes strong resonant coupling, further enhanced by the near-field effect, which increases the thermal radiation density of states.[56] Weyl semimetals include the chiral magnetic effect and the anomalous Hall effect, which can be described within the framework of axion electrodynamics. Axion electrodynamics introduces an additional term in the electromagnetic Lagrangian density

$$\mathcal{L}_\theta = 2\alpha\sqrt{\frac{\varepsilon_0}{\mu_0}}\frac{\theta(\boldsymbol{r},t)}{2\pi}\boldsymbol{E}\cdot\boldsymbol{B}, \tag{1}$$

where $\alpha = e^2/4\pi\epsilon_0\hbar c$ is the fine structure constant, $\boldsymbol{E}$ is the electric field, $\boldsymbol{B}$ is the magnetic flux density, and $\theta(\boldsymbol{r},t)$ is the axion angle that depends on space and time.[43]

The permittivity tensor of such a Weyl semimetal is[41,43]

$$\bar{\bar{\varepsilon}}_{\mathrm{Weyl}} = \begin{bmatrix} \varepsilon_{\mathrm{d}} & \mathrm{i}\varepsilon_{\mathrm{a}} & 0 \\ -\mathrm{i}\varepsilon_{\mathrm{a}} & \varepsilon_{\mathrm{d}} & 0 \\ 0 & 0 & \varepsilon_{\mathrm{d}} \end{bmatrix}, \tag{2}$$

where $\varepsilon_{\mathrm{a}} = be^2/2\pi^2\hbar\omega$ is the off-diagonal term responsible for breaking Lorentz reciprocity. This nonreciprocity

arises from the intrinsic anomalous Hall effect induced by the Berry curvature associated with the Weyl nodes, without requiring any external magnetic field.

To calculate the diagonal term $\varepsilon_{\rm d}$, we apply the Kubo–Greenwood formalism within the random phase approximation to a two-band model with spin degeneracy. This formalism takes into account both interband and intraband transitions,

$$\varepsilon_{\rm d} = \varepsilon_{\rm b} + {\rm i}\frac{\sigma}{\omega}, \tag{3}$$

where $\varepsilon_{\rm b}$ is the background permittivity and σ is the bulk conductivity and given by [43]

$$\sigma = \frac{r_{\rm s} g}{6}\Omega\, G(\Omega/2) + {\rm i}\frac{r_{\rm s} g}{6\pi}\Big\{\frac{4}{\Omega}\Big[1+\frac{\pi^2}{3}\Big(\frac{k_{\rm B}T}{E_{\rm f}(T)}\Big)^2\Big] + 8\Omega\int_0^{\xi_{\rm c}}\frac{G(\xi)-G(\Omega/2)}{\Omega^2-4\xi^2}\xi{\rm d}\xi\Big\}, \tag{4}$$

where $E_{\rm f}(T)$ is the chemical potential, $\Omega = \hbar(\omega+{\rm i}\tau^{-1})/E_{\rm f}$ is the complex frequency normalized by the chemical potential, τ^{-1} is the scattering rate corresponding to Drude damping, $G(E) = f(-E) - f(E)$, where $f(E)$ is the Fermi distribution function, $r_{\rm s} = e^2/4\pi\varepsilon_0\hbar v_{\rm F}$ is the effective fine structure constant, $v_{\rm F}$ is the Fermi velocity, g is the number of Weyl points, and $\xi_{\rm c} = E_{\rm c}/E_{\rm f}$ where $E_{\rm c}$ is the cutoff energy beyond which the band dispersion is no longer linear. In this work, we use the parameters $\varepsilon_{\rm b} = 6.2$, $\xi_{\rm c} = 3$, $\tau = 1000\,{\rm fs}$, $g = 2$, and $v_{\rm F} = 0.83\times10^5\,{\rm m/s}$.

The dielectric function of the InSb cell is given by [57]

$$\varepsilon_{\rm InSb} = \Big(n + {\rm i}\frac{c\alpha(\omega)}{2\omega}\Big)^2, \tag{5}$$

where $n = 4.12$ is the refractive index and c is the speed of light in vacuum. $\alpha(\omega)$ is a step-like function which describes the absorption probability of the incident photons, and it is given by $\alpha(\omega) = 0$ for $\omega < \omega_{\rm g}$ and $\alpha(\omega) = \alpha_0\sqrt{\omega/\omega_{\rm gap}-1}$ for $\omega > \omega_{\rm g}$ with $\alpha_0 = 0.7\,\mu{\rm m}^{-1}$ being the absorption coefficient and $\omega_{\rm g} = E_{\rm g}/\hbar$ being the angular frequency corresponding to the band gap of InSb. The gap energy $E_{\rm g}$ of InSb is temperature dependent, which is given by $E_{\rm g} = 0.24 - 6\times10^{-4}T^2/(T+500)$. [58] For instance, for $T_{\rm c} = 320\,{\rm K}$, the gap energy $E_{\rm g}$ is nearly $0.17\,{\rm eV}$ and the corresponding frequency is about $2.5\times10^{14}\,{\rm Hz}$.

The near-field radiative heat flux exchanged between the emitter and the cell is given by fluctuational electrodynamics, [59,60]

$$Q_{\rm rad}(T_{\rm e},T_{\rm c},\omega,\Delta\mu) = \int_0^\infty\frac{{\rm d}\omega}{4\pi^2}[\Theta(T_{\rm e},\omega,0)-\Theta(T_{\rm c},\omega,\Delta\mu)] \times\sum_j\int_0^{2\pi}\int_0^\infty\zeta(\omega,k,\phi)k{\rm d}k{\rm d}\phi, \tag{6}$$

where $\Theta(T,\omega,\Delta\mu) = \hbar\omega/[\exp(\hbar\omega-\Delta\mu/k_{\rm B}T)-1]$ is the Planck mean oscillator energy of blackbody at temperature T. $\Delta\mu$ is the electrochemical potential difference across the p–n junction in the thermophotovoltaic cell. k denotes the magnitude of the in-plane wavevector of thermal radiation waves and ϕ is the azimuthal angle. $\zeta(\omega,k,\phi)$ is called the photon transmission coefficient, which describes the probability for photons tunneling across the vacuum gap from the emitter to the cell (see Supplementary Materials).

When the thermophotovolatic cell is located at a distance d which is on the order of or smaller than the thermal wavelength $\lambda_{\rm th} = 2\pi\hbar c/k_{\rm B}T_{\rm e}$ from the emitter, the radiative energy transfer will be enhanced due to the presence of evanescent waves. [61] The enhanced radiation with energy greater than the band gap $E_{\rm g}$ will be absorbed by the thermophotovolatic cell, creating electron–hole pairs and leading to electric current flow and output power generation. The induced electric current density can be written as [62,63]

$$I_{\rm e} = I_{\rm ph} - I_0[\exp(V/V_{\rm c})-1], \tag{7}$$

where $V = \Delta\mu/e$ is the voltage bias across the thermophotovoltaic cell, [62] $V_{\rm c} = k_{\rm B}T_{\rm c}/e$ is a voltage which measures the temperature of the cell. [62] $I_{\rm ph}$ and I_0 are called the photo-induced current density and reverse saturation current density, respectively. The reverse saturation current density is determined by the diffusion of minority carriers in the InSb p–n junction, which is given by

$$I_0 = en_{\rm i}^2\Big(\frac{1}{N_{\rm A}}\sqrt{\frac{D_{\rm e}}{\tau_{\rm e}}}+\frac{1}{N_{\rm D}}\sqrt{\frac{D_{\rm h}}{\tau_{\rm h}}}\Big), \tag{8}$$

where $n_{\rm i} = \sqrt{N_{\rm c}N_{\rm v}}\exp(-E_{\rm g}/2k_{\rm B}T_{\rm c})$ $({\rm cm}^{-3})$ is the intrinsic carrier concentration, which is dependent on the temperature of the thermophotovoltaic cell. [58] $N_{\rm c}$ and $N_{\rm v}$ are temperature-dependent effective density of states in the conduction and valance bands given by $N_{\rm c} = 8\times10^{12}\times T_{\rm c}^{\frac{3}{2}}$ $({\rm cm}^{-3})$ and $N_{\rm v} = 1.4\times10^{15}\times T_{\rm c}^{\frac{3}{2}}$ $({\rm cm}^{-3})$, respectively. $N_{\rm A}$ ($N_{\rm D}$) is the p-region (n-region) impurity concentration. Numerical values are set as $N_{\rm A} = N_{\rm D} = 10^{19}$ $({\rm cm}^{-3})$. $D_{\rm e}$ and $D_{\rm h}$ are the diffusion coefficients of the electrons and holes, taken as $D_{\rm e} = 186\,{\rm cm}^2/{\rm s}$ and $D_{\rm h} = 5.21\,{\rm cm}^2/{\rm s}$. [7] $\tau_{\rm e}$ and $\tau_{\rm h}$ are the relaxation times of the electron–hole pairs in the n-region and p-region, correspondingly. [64]

Photo-induced current is the electric current induced by the motion of photo-carriers. The photo-induced current density $I_{\rm ph}$ is given by [64]

$$I_{\rm ph} = e\int_{\omega_{\rm g}}^\infty\frac{Q_{\rm rad}(T_{\rm e},T_{\rm c},\omega,\Delta\mu)}{\hbar\omega}{\rm d}\omega, \tag{9}$$

where the radiative spectral heat flux is defined in Eq. (6). Here we assume that all incident photons are absorbed, and each photon with energy greater than the band gap creates one electron–hole pair, i.e., we assume 100% quantum efficiency. [57] Under this assumption, we only consider the energy efficiency, which measures how much incident radiative heat can be transferred into electricity. We keep this assumption which is widely adopted in literatures.

The output electric power density $P_{\rm e}$ is defined as the product of the net electric current density and the voltage bias. The energy efficiency η is given by the ratio between the output electric power density $P_{\rm e}$ and incident radiative heat flux $Q_{\rm inc}$,

$$P_{\rm e} = -I_{\rm e}V, \quad \eta = \frac{P_{\rm e}}{Q_{\rm inc}}, \tag{10}$$

where the incident radiative heat flux is given by

$$
\begin{aligned}
Q_{\mathrm{inc}} &= \int_0^{\infty} Q_{\mathrm{rad}}(T_{\mathrm{e}}, T_{\mathrm{cell}}, \omega, \Delta\mu)\mathrm{d}\omega \\
&= \int_0^{\infty} \frac{\mathrm{d}\omega}{(2\pi)^3}\Theta_1(T_{\mathrm{e}}, \omega)\int_0^{2\pi}\int_0^{\infty}\zeta(\omega, k, \phi)k\mathrm{d}k\mathrm{d}\phi \\
&- \int_{\omega_{\mathrm{g}}}^{\infty} \frac{\mathrm{d}\omega}{(2\pi)^3}\Theta_2(T_{\mathrm{c}}, \omega, \Delta\mu)\int_0^{2\pi}\int_0^{\infty}\zeta(\omega, k, \phi)k\mathrm{d}k\mathrm{d}\phi \\
&- \int_0^{\omega_{\mathrm{g}}} \frac{\mathrm{d}\omega}{(2\pi)^3}\Theta_1(T_{\mathrm{c}}, \omega)\int_0^{2\pi}\int_0^{\infty}\zeta(\omega, k, \phi)k\mathrm{d}k\mathrm{d}\phi. \quad (11)
\end{aligned}
$$

3. Results and Discussions. Figure 2(a) shows the electric power density P_{e} as a function of voltage V for various chemical potentials, while maintaining equal chemical potential values in the two layers of Weyl semimetals. The red curve, corresponding to a chemical potential of $E_{\mathrm{f},1(3)} = 0.2\,\mathrm{eV}$, reaches its maximum power density $P_{\mathrm{e}} = 6.5\times10^4\,\mathrm{W\cdot m^{-2}}$ at a voltage of $V = 0.035\,\mathrm{eV}$. As the chemical potential is increased to $E_{\mathrm{f},1(3)} = 0.21\,\mathrm{eV}$, the maximum power density decreases to $P_{\mathrm{e}} = 5.8\times10^4\,\mathrm{W\cdot m^{-2}}$, with a slight increase in the cutoff voltage. Further increasing the chemical potential to $E_{\mathrm{f},1(3)} = 0.25\,\mathrm{eV}$ results in a significant drop in maximum power density to $P_{\mathrm{e}} = 2.3\times10^4\,\mathrm{W\cdot m^{-2}}$, and the cutoff voltage increases further to $V = 0.06\,\mathrm{eV}$. This trend illustrates how higher chemical potentials reduce the maximum achievable power density and shift the voltage at which the maximum power occurs. Figure 2(b) shows the energy efficiency of the NTPV systems as a function of voltage for different chemical potentials, specifically for $E_{\mathrm{f},1(3)} = 0.2\,\mathrm{eV}$, $E_{\mathrm{f},1(3)} = 0.21\,\mathrm{eV}$, and $E_{\mathrm{f},1(3)} = 0.25\,\mathrm{eV}$. For the lower chemical potentials of $E_{\mathrm{f},1(3)} = 0.2\,\mathrm{eV}$ and $E_{\mathrm{f},1(3)} = 0.21\,\mathrm{eV}$, the output efficiency increases to about 60% of the Carnot efficiency (η_{C}), with the latter slightly outperforming the former. However, when the chemical potential is increased further to $E_{\mathrm{f},1(3)} = 0.25\,\mathrm{eV}$, the output efficiency drops significantly to around 50% of the Carnot efficiency, which represents the minimum value in this study. This trend emphasizes the crucial role of the chemical potential in modulating the efficiency of NTPV systems. As the value increases, efficiency decreases, suggesting that higher chemical potentials introduce electronic characteristics that hinder efficient energy conversion. Thus, optimizing the chemical potential is crucial for maximizing the performance of NTPV systems.

Figures 2(c) and 2(d) illustrate how different chemical potential configurations affect output power and energy efficiency in a sandwich structure made of Weyl semimetals. Figure 2(c) shows how the output power depends on the chemical potentials, similar to what is shown in Fig. 2(a). However, figure 2(d) demonstrates that when the chemical potential of layer 1 is slightly different from that of layer 3, the maximum energy efficiency can be increased from 60.5% to 65% of Carnot efficiency. To further explore such efficiency enhancement effect, figure 3(a) shows the spectral distributions Q_{inc} with different chemical potential configurations. As the chemical potential in layer 1 increases, the resonance peak splits into two distinct peaks, and the magnitude of the peak diminishes with

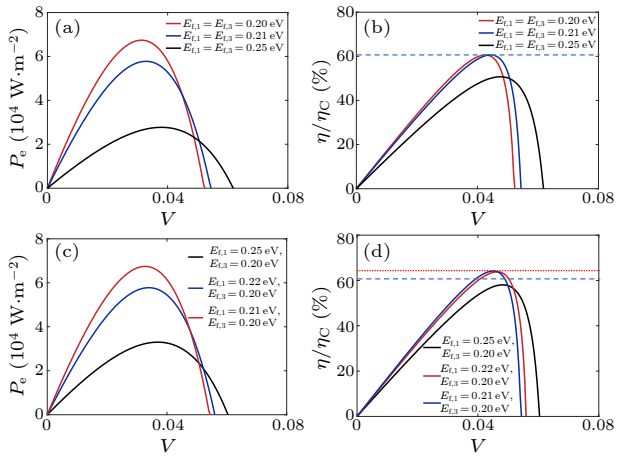

Fig. 2. Performances of the NTPV systems at different chemical potentials of the Weyl semimetals. (a) and (c) The output power P_{e} as a function of V for $E_{\mathrm{f},1} = E_{\mathrm{f},3}$ and $E_{\mathrm{f},1} \neq E_{\mathrm{f},3}$, respectively. (c) and (d) The energy-conversion efficiency η/η_{C} as a function of V for $E_{\mathrm{f},1} = E_{\mathrm{f},3}$ and $E_{\mathrm{f},1} \neq E_{\mathrm{f},3}$, respectively. The parameters are: $T_{\mathrm{e}} = 450\,\mathrm{K}$, $T_{\mathrm{c}} = 320\,\mathrm{K}$, $d = 20\,\mathrm{nm}$, $h_{\mathrm{W}} = 20\,\mathrm{nm}$, $h_0 = 10\,\mathrm{nm}$, $h_{\mathrm{InSb}} = 10000\,\mathrm{nm}$.

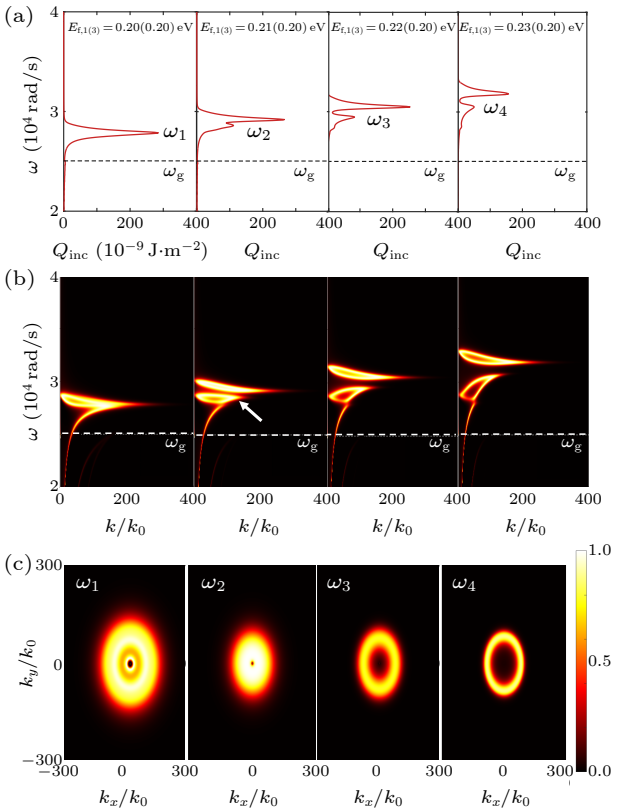

Fig. 3. (a) Spectral distributions Q_{inc}. (b) and (c) The photon transmission coefficients of the NTPV systems for different chemical potentials in the ω–k plane and k_x–k_y plane, respectively. The other parameters are the same as those in Fig. 2.

this increase in chemical potential. When $E_{\mathrm{f},1} = 0.21\,\mathrm{eV}$, we observed that the overall width of the two peaks and total flux increased compared to $E_{\mathrm{f},1} = 0.20\,\mathrm{eV}$, i.e., the resonance condition. This broadening is also evident in the transmission coefficient distribution, where more states

contribute to photon transmission above the bandgap. The dispersion of surface plasmons in Weyl semimetals is strongly affected by the chemical potential. Varying chemical potentials results in the dispersion of surface plasmons occurring at different frequency positions. Figure 3(b) illustrates the photon transmission coefficient of the NTPV systems at varying chemical potentials. Our findings reveal that the dislocation effect occurring between different chemical potentials across Weyl layers leads to the formation of quasi-flat bands in momentum space.

Figure 3(c) shows the transmission coefficient ξ as a function of the wavevector components k_x and k_y at peak frequency with different band dislocation effects. Compared with the third and fourth figures in Fig. 3(c), the second figure in Fig. 3(c) illustrates a more noticeable resonance effect due to the smaller band dislocation. This means that the proper band dislocations facilitate the creation of an effective heat transfer channel. This broadening effect in the k space is the key reason why the presence of dislocations, represented by the chemical potential mismatch, leads to a substantial enhancement in both the efficiency and power output of the NTPV cells. The shift in energy alignment as a result of the band dislocation allows a wider range of photon energies to participate in radiative heat transfer, effectively increasing the available thermal energy for conversion. Furthermore, enhanced photon transmission above the bandgap ensures that more high-energy photons contribute to electron excitation in the photovoltaic cell, thereby improving both power generation and energy conversion efficiency. These findings highlight the crucial role of chemical potential engineering in optimizing NTPV systems, demonstrating that controlled dislocations or engineered energy level mismatches can be an effective strategy for enhancing performance beyond conventional configurations with symmetric chemical potentials.

To further enhance the performance of the NTPV system, we focus on optimizing key parameters that significantly influence the system's energy-converison efficiency and output power in Fig. 4. Specifically, we adjust the thickness h_{WSM} of the Wely semimetals and the voltage bias V. From the figure, we observe that when the thickness of the Weyl semimetals exceeds 14 nm and the symmetric chemical potential E_{f} is below 0.05 eV,

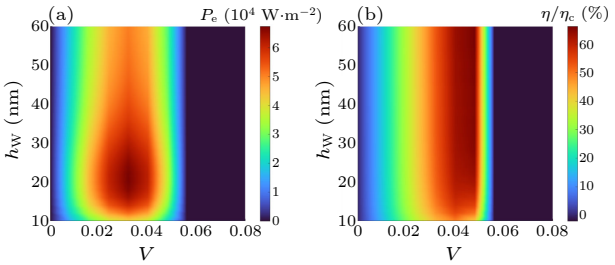

Fig. 4. Optimized performances of the NTPV system. (a) Electric power density P_{e} (b) Energy-conversion efficiency in units of Carnot efficiency (η/η_{c}) as functions of the thickness h_{W} of the Wely semimetals and voltage bias V. The parameters are: $T_{\mathrm{e}} = 450\,\mathrm{K}$, $T_{\mathrm{c}} = 320\,\mathrm{K}$, $d = 20\,\mathrm{nm}$, $h_0 = 10\,\mathrm{nm}$, $h_{\mathrm{InSb}} = 10000\,\mathrm{nm}$, $E_{\mathrm{f},1} = 0.21\,\mathrm{eV}$ and $E_{\mathrm{f},3} = 0.20\,\mathrm{eV}$.

both the output power and the energy efficiency reach their optimal values. In particular, the power reaches $7 \times 10^4\,\mathrm{W{\cdot}m^{-2}}$ while the efficiency achieves 65% of the Carnot efficiency. This demonstrates a clear tuning window where both performance metrics are significantly improved. Within this parameter range, the emitter and absorber are optimally coupled, which originates from the coupling between the electron-hole excitations in the InSb p–n junction and the surface-plasmon polaritons in the Weyl semimetals.

4. Summary and Outlook. In this work, we propose and optimize an NTPV system based on magnetic Weyl semimetals, aiming to enhance the performance of thermophotovoltaic cells. Our results indicate that tuning the chemical potential and carefully adjusting the geometrical and material parameters can lead to a substantial enhancement in the output power and efficiency of the NTPV systems. Specifically, by modifying the displacement of the chemical potentials, we observed shifts in the resonant frequencies of the photon tunneling bands and enhancements of the NTPV systems with band dislocation. It is also found that there is an optimal Weyl layer thickness to ensure high power and efficiency. Future research on InSb absorption spectra should integrate advanced spectroscopic techniques, first-principles calculations, and nanostructure engineering to unlock its potential in infrared optoelectronics and quantum technologies.[65,66] Emerging quantum materials such as charge-density-wave systems and borophene demonstrate significant potential as next-generation thermophotovoltaic emitters, owing to their exceptional tunability in near-field radiative heat transfer and enhanced thermal energy conversion capabilities.[67–69] Our work opens new avenues for developing high-performance thermal emitters and photovoltaic cells that can find applications in waste heat recovery, solar energy conversion, and other energy harvesting technologies.

Acknowledgments. This work was supported by the National Natural Science Foundation of China (Grant Nos. 12125504 and 12305050), the National Key R&D Program of China (Grant No. 2022YFA1404400), the Hundred Talents Program of the Chinese Academy of Sciences, the Natural Science Foundation of Jiangsu Higher Education Institutions of China (Grant No. 23KJB140017), the Opening Project of Shanghai Key Laboratory of Special Artificial Microstructure Materials and Technology (Grant No. Ammt2023B-1), and the Guangdong University of Technology SPOE Seed Foundation (Grant No. SF2024111502).

References

[1] Martın D and Algora C 2004 *Semicond. Sci. Tech.* **19** 1040

[2] Datas A and Martı A 2017 *Sol. Energy Mater.* **161** 285

[3] Mittapally R, Majumder A, Reddy P, and Meyhofer E 2023 *Phys. Rev. Appl.* **19** 037002

[4] Park Y, Omair Z, and Fan S 2022 *ACS Photonics* **9** 3943

[5] Bhatt G R, Zhao B, Roberts S, Datta I, Mohanty A, Lin T, Hartmann J M, St-Gelais R, Fan S, and Lipson M 2020 *Nat. Commun.* **11** 2545
[6] Chen S, Guo Y, Pan Q, and Shuai Y 2024 *Int. J. Extreme Manuf.* **6** 022009
[7] Lim M, Jin S, Lee S S, and Lee B J 2015 *Opt. Express* **23** A240
[8] Tervo E, Bagherisereshki E, and Zhang Z M 2018 *Front. Energy* **12** 5
[9] Zhao B, Chen K, Buddhiraju S, Bhatt G, Lipson M, and Fan S 2017 *Nano Energy* **41** 344
[10] Liao T, Cai L, Zhao Y, and Chen J 2016 *J. Power Sources* **306** 666
[11] Song J, Han J, Choi M, and Lee B J 2022 *Sol. Energy Mater. Sol. Cells* **238** 111556
[12] Burger T, Sempere C, Roy-Layinde B, and Lenert A 2020 *Joule* **4** 1660
[13] Li X, Lou C, Li X, Zhang Y, Liu Z, and Yin B 2020 *Phys. Rev. Appl.* **13** 041002
[14] Biehs S A, Messina R, Venkataram P S, Rodriguez A W, Cuevas J C, and Ben-Abdallah P 2021 *Rev. Mod. Phys.* **93** 025009
[15] Tachikawa S, Ordonez-Miranda J, Jalabert L, Wu Y, Anufriev R, Guo Y, Kim B, Fujita H, Volz S, and Nomura M 2024 *Phys. Rev. Lett.* **132** 186904
[16] Chan W R, Bermel P, Pilawa-Podgurski R C N, Marton C H, Jensen K F, Senkevich J J, Joannopoulos J D, Soljacic M, and Celanovic I 2013 *Proc. Nat. Acad. Sci.* **110** 5309
[17] Odebowale A A, Berhe A, Ogundare R T, Abdo S, Abdulghani A, Hattori H T, and Miroshnichenko A E 2025 *Adv. Funct. Mater.* **35** 2421051
[18] Song J and Cheng Q 2016 *Phys. Rev. B* **94** 125419
[19] Lu Q, Zhou X, Krysa A, Marshall A, Carrington P, Tan C H, and Krier A 2018 *Sol. Energy Mater. Sol. Cells* **179** 334
[20] Lu Q, Beanland R, Montesdeoca D, Carrington P J, Marshall A, and Krier A 2019 *Sol. Energy Mater. Sol. Cells* **191** 406
[21] Song J, Cheng Q, Lu L, Li B, Zhou K, Zhang B, Luo Z, and Zhou X 2020 *Phys. Rev. Appl.* **13** 024054
[22] Mittapally R, Lee B, Zhu L, Reihani A, Won Lim J, Fan D, Forrest S R, Reddy P, and Meyhofer E 2021 *Nat. Commun.* **12** 4364
[23] Lu L, Zhang B, Ou H, Li B, Zhou K, Song J, Luo Z, and Cheng Q 2022 *Small* **18** 2108032
[24] Song J, Jang J, Lim M, Choi M, Lee J, and Lee B J 2022 *ACS Photonics* **9** 1748
[25] Li S, Xu D, Zhao J, and Liu L 2023 *Int. J. Heat Mass Transfer* **202** 123713
[26] Choi M, Song J, and Lee B J 2024 *Int. Commun. Heat Mass Transfer* **153** 107355
[27] Zhao B and Zhang Z M 2015 *J. Heat Transfer* **139** 022701
[28] Wu X and Fu C J 2021 *J. Quant. Spectrosc. Radiat. Transf.* **258** 107337
[29] Liu X and Xuan Y 2016 *Sci. China Technol. Sci.* **59** 1680
[30] He M J, Guo X, Qi H, Zheng Z H, Antezza M, and Tan H P 2023 *Phys. Chem. Chem. Phys.* **25** 20782
[31] Zhou C, Yang S H, Zhang Y, and Yi H L 2020 *Nanoscale Microscale Thermophys. Eng.* **24** 168
[32] Zhang Y, Zhou C L, Qu L, and Yi H L 2020 *Appl. Phys. Lett.* **116** 151101
[33] Brar V W, Jang M S, Sherrott M, Kim S, Lopez J J, Kim L B, Choi M, and Atwater H 2014 *Nano Lett.* **14** 3876
[34] Tang L, DeSutter J, and Francoeur M 2020 *ACS Photonics* **7** 1304
[35] Peng J, Tang G, Wang L, Macedo R, Chen H, and Ren J 2021 *ACS Photonics* **8** 2183
[36] Papadakis G T, Buddhiraju S, Zhao Z, Zhao B, and Fan S 2020 *Nano Lett.* **20** 1654
[37] Li B and Cheng Q 2023 *AIP Conf. Proc.* **2841** 070001
[38] Wang R, Lu J, Wu X, Peng J, and Jiang J H 2023 *Phys. Rev. Appl.* **19** 044050
[39] Li L, Wu X, Liu H, Yang Z, Liu Y, and Yu K 2024 *Int. J. Heat Mass Transfer* **230** 125783
[40] Biehs S A, Tschikin M, and Ben-Abdallah P 2012 *Phys. Rev. Lett.* **109** 104301
[41] Zyuzin A A and Burkov A A 2012 *Phys. Rev. B* **86** 115133
[42] Kotov O V and Lozovik Y E 2018 *Phys. Rev. B* **98** 195446
[43] Zhao B, Guo C, Garcia C A, Narang P, and Fan S 2020 *Nano Lett.* **20** 1923
[44] Wan X, Turner A M, Vishwanath A, and Savrasov S Y 2011 *Phys. Rev. B* **83** 205101
[45] Armitage N P, Mele E J, and Vishwanath A 2018 *Rev. Mod. Phys.* **90** 015001
[46] Wang H X, Lin Z K, Jiang B, Guo G Y, and Jiang J H 2020 *Phys. Rev. Lett.* **125** 146401
[47] Tsurimaki Y, Qian X, Pajovic S, Han F, Li M, and Chen G 2020 *Phys. Rev. B* **101** 165426
[48] Pajovic S, Tsurimaki Y, Qian X, and Chen G 2020 *Phys. Rev. B* **102** 165417
[49] Tang G, Chen J, and Zhang L 2021 *ACS Photonics* **8** 443
[50] Guo C, Zhao B, Huang D, and Fan S 2020 *ACS Photonics* **7** 3257
[51] Lucchesi C, Cakiroglu D, Perez J P, Taliercio T, Tournie E, Chapuis P O, and Vaillon R 2021 *Nano Lett.* **21** 4524
[52] Mittapally R, Lee B, Zhu L, Reihani A, Lim J W, Fan D, Forrest S R, Reddy P, and Meyhofer E 2021 *Nat. Commun.* **12** 4364
[53] Zhang Z M 2007 *Nano/Microscale Heat Transfer* (Springer Cham)
[54] Zhang J, Zhang T, Yan L *et al.* 2022 *Adv. Mater.* **34** 2204621
[55] Song J, Yao X, Jin L, Chen L, Zhao H, and Cheng Q 2024 *Sci. China Technol. Sci.* **67** 3405
[56] Li L, Yu K, Feng D, Yang Z, Zhang K, Liu Y, and Wu X 2023 *Phys. Rev. Appl.* **20** 064015
[57] Messina R and Ben-Abdallah P 2013 *Sci. Rep.* **3** 1383
[58] Shur M S 1996 *Handbook series on semiconductor parameters* (World Scientific)
[59] Polder D and Van Hove M 1971 *Phys. Rev. B* **4** 3303
[60] Pendry J B 1999 *J. Phys.: Condens. Matter* **11** 6621
[61] Ilic O, Jablan M, Joannopoulos J D, Celanovic I, and Soljacic M 2012 *Opt. Express* **20** A366
[62] Shockley W and Queisser H J 1961 *J. Appl. Phys.* **32** 510
[63] Ashcroft N W and Mermin N D 1976 *Solid state physics* (Cengage Learning)
[64] Laroche M, Carminati R, and Greffet J J 2006 *J. Appl. Phys.* **100** 063704
[65] Schaefer S T, Gao S, Webster P T, Kosireddy R R, and Johnson S R 2020 *J. Appl. Phys.* **127** 165705
[66] Song J, Cheng Q, Zhang B, Lu L, Zhou X, Luo Z, and Hu R 2021 *Rep. Prog. Phys.* **84** 036501
[67] Balandin A A, Zaitsev-Zotov S V, and Gruner G 2021 *Appl. Phys. Lett.* **119** 170401
[68] Kaneti Y V, Benu D P, Xu X, Yuliarto B, Yamauchi Y, and Golberg D 2022 *Chem. Rev.* **122** 1000
[69] Adekoya G J, Adekoya O C, Muloiwa M, Sadiku E R, Kupolati W K, and Hamam Y 2024 *Small* **20** 2403656